Supplementary Information

"Moraine crest or slope: an analysis of the effects of boulder position on cosmogenic exposure age"

Matt D. Tomkins[1,2], Jason M. Dortch[3], Philip D. Hughes[1,2], Jonny J. Huck[1], Raimon Pallàs[4], Ángel Rodés[5], James L. Allard[1,2], Andrew G. Stimson[1,2], Didier Bourlès[6], Vincent Rinterknecht[6], Vincent Jomelli[6], Laura Rodríguez-Rodríguez[7], Ramon Copons[8], Iestyn D. Barr[9,2], Christopher M. Darvill[1,2] and Thomas Bishop[1]

1 *Department of Geography, University of Manchester,* ***2*** *Cryosphere Research at Manchester,* ***3*** *Kentucky Geological Survey, University of Kentucky,* ***4*** *Departament de Dinàmica de la Terra i de l'Oceà, Universitat de Barcelona,* ***5*** *Scottish Universities Environmental Research Centre,* ***6*** *Aix-Marseille Univ., CNRS,* ***7*** *Dpto. Ciencias de la Tierra y Física de la Materia Condensada, Universidad de Cantabria,* ***8*** *Snow and Mountain Research Centre of Andorra (CENMA), Andorran Research Institute (IEA),* ***9*** *Department of Natural Sciences, Manchester Metropolitan University*

Contents

Page

List of Figures **2**

List of Tables **3**

1 ^{10}Be analysis **4**
1.1 Landform age analysis 6

2 Sensitivity analysis **9**
2.1 Methods 9
2.2 Results 12

3 Boulder characteristics **14**
3.1 Methods 14
3.2 Results 15

4 Monte Carlo ODR **20**

5 Supplementary Tables **24**
5.1 Supplementary Tables 1-2 24
5.2 Supplementary Table 3 27

Bibliography **34**

List of Figures

		Page
S1	Sample photos of ^{10}Be dated boulders on the Arànser right moraine	5
S2	P-CAAT analysis of ^{10}Be and ^{36}Cl ages on the Arànser right moraine	7
S3	Schematic for boulder classification	9
S4	Histograms of simulated landform ages	11
S5	Minimum sample sizes based on 1σ and 2σ thresholds.	13
S6	Histogram of boulder sphericity values	15
S7	Significant predictors following inter-landform scale logistic regression	17
S8	Significant predictors following logistic regression of the Arànser left dataset	19
S9	TCN age-uncertainty collinearity.	21
S10	^{10}Be measurement uncertainties.	22
S11	Simulated model coefficients from Orthogonal Distance Regression	23
S12	Outliers and new calibration data for the Pyrenean TCN-SH calibration curve	25
S13	ODR TCN-SH calibration curve	28

List of Tables

Page

T1 P-CAAT input for the Arànser right moraine 6
T2 Results of sensitivity analysis 12
T3 Results of logistic regression of boulder characteristics 16

1 | ^{10}Be analysis

10 boulders were selected on the Arànser right moraine for ^{10}Be analysis (*see* Fig. S1). Sample treatment was performed at the Laboratori de Cosmonúclids Terrestres de la Universitat de Barcelona, Spain. All samples were crushed and sieved in order to isolate the 250–710 µm fraction. The quartz fraction was separated and purified using magnetic separation and mineral flotation techniques prior to chemical etching procedures modified from Kohl and Nishiizumi (1992). Quartz purity was assayed using ICP-OES. Up to 450 µm of a commercial ^{9}Be carrier (Scharlau) was added to each sample. Beryllium extraction was carried out using methods modified from Child et al. (2000).

Measurements of isotope ratios in the samples and two procedural blanks were performed at ASTER, the French Accelerator Mass Spectrometer located at CEREGE, Aix-en-Provence, France. Data were normalised against the National Institute of Standards and Technology (NIST) standard reference material 4325 using an assigned ^{10}Be/^{9}Be ratio of $2.79 \pm 0.03 \times 10^{-11}$ (Nishiizumi et al., 2007) and a ^{10}Be half-life of $1.387 \pm 0.012 \times 10^{6}$ years (Chmeleff et al., 2010; Korschinek et al., 2010). Analytical uncertainties (reported as 1σ) include uncertainties associated with AMS counting statistics, AMS external error and chemical blank measurement. ^{10}Be concentrations in quartz were calculated following Balco (2006) and exposure ages calculated using the CRONUS Earth Web Calculator (Marrero et al., 2016). All ages are reported with no correction for erosion or snow cover to ensure that they are treated as minimum ages of exposure.

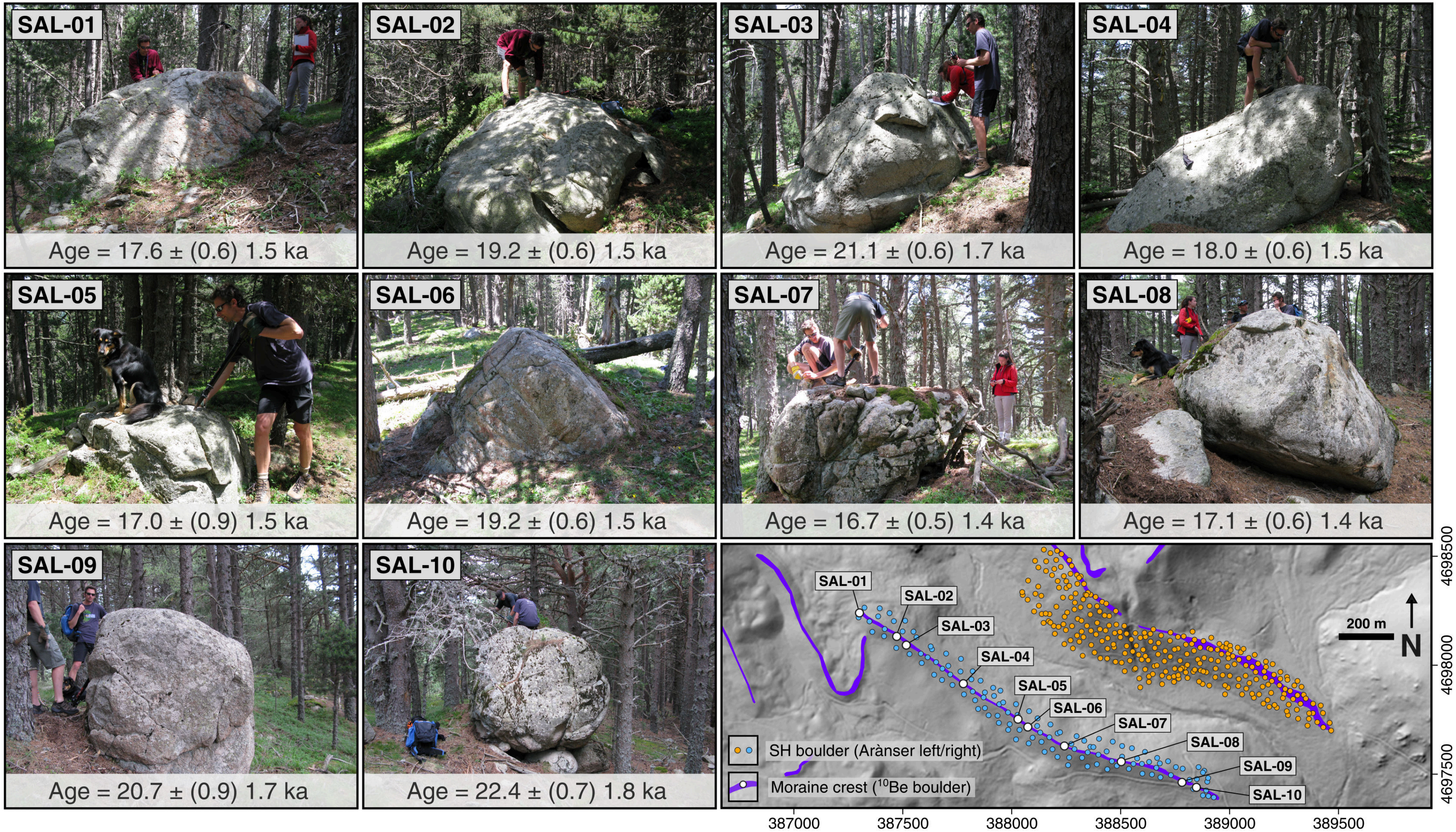

Figure S1: Sample photos of ^{10}Be dated boulders on the Arànser right moraine (SAL-01 to SAL-10) and their corresponding exposure ages (ka) ± (internal) external uncertainties. Their locations are shown on the inset map (Topographic hillshade based on a ~5 m DEM from the Instituto Geográfico Nacional), in addition to SH sampled boulders on the Arànser left (orange points; n = 275) and right moraines (blue circles; n = 130).

1.1 Landform age analysis

Full sample information used for age calculation and landform age analysis are provided in Supplementary Table 1 (described below in Section 5). Table T1 includes the corresponding input data for P-CAAT (Dortch et al., 2019).

Table T1: P-CAAT input for the Arànser right moraine

Sample name	Isotope	Age (ka)	Internal ± (ka)	External ± (ka)
SAL-01	^{10}Be	17.6	0.6	1.5
SAL-02	^{10}Be	19.2	0.6	1.5
SAL-03	^{10}Be	21.1	0.6	1.7
SAL-04	^{10}Be	18.0	0.6	1.5
SAL-05	^{10}Be	17.0	0.9	1.6
SAL-06	^{10}Be	19.2	0.6	1.5
SAL-07	^{10}Be	16.7	0.5	1.4
SAL-08	^{10}Be	17.1	0.6	1.4
SAL-09	^{10}Be	20.7	0.9	1.7
SAL-10	^{10}Be	22.4	0.7	1.8
PIR-11-13	^{36}Cl	18.2	1.6	2.1
PIR-11-14	^{36}Cl	17.3	1.7	2.2

The distribution of these data is skewed (0.67) and non-normal, as assessed using a Shapiro-Wilk test (W = 0.90, p = 0.14). Calculated ages range from 17.0 ± 1.6 ka (SAL-05) to 22.4 ± 1.8 ka (SAL-10). The arithmetic mean ± total uncertainty is 18.7 ± 1.9 ka, where total uncertainty (t) is equal to:

$$t = \sqrt{GU^2 + SU^2}$$

where systematic uncertainty (SU) incorporates measurement errors:

$$SU = \frac{\sqrt{Sum\,of\,the\,squared\,errors}}{Number\,of\,observations}$$

and where geologic uncertainty (GU) incorporates the clustering of the dataset, which is typically interpreted as the effects of pre- and post-depositional processes that modify cosmogenic nuclide concentrations:

$$GU = Standard\ deviation$$

Using P-CAAT, and selecting the oldest component Gaussian distribution that contains ≥ 3 ages to represent the age of the landform (*see* Fig. 3 in Dortch et al., 2013), these data return a landform age of 21.5 ± 2.2 ka (Fig. S2; $n = 12$; Mean bandwidth estimator; Numeric bandwidth = 0.8108, $R^2 = 0.9997$, $p < 0.01$). This estimate is consistent within measurement uncertainties with the SH-derived landform ages for both the Arànser right (22.3 ± 0.9 ka) and left moraines (23.3 ± 1.1 ka) and is based on standard procedures for interpreting moraine ages as minimum limiting ages (Putkonen and Swanson, 2003; Briner et al., 2005).

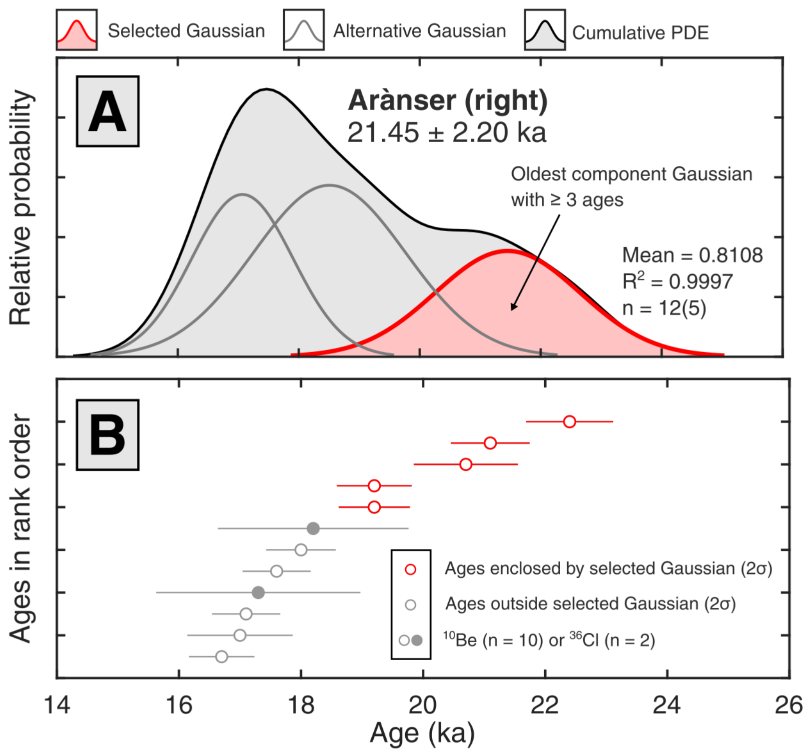

Figure S2: P-CAAT analysis of ^{10}Be ($n = 10$) and ^{36}Cl ($n = 2$) ages on the Arànser right moraine (Dortch et al., 2019). (A) Cumulative probability density estimate (PDE) and component Gaussian distributions. Following the approach of Dortch et al. (2013), we select the oldest Gaussian with contains ≥ 3 ages to represent the age of the landform. (B) Individual ^{10}Be and ^{36}Cl ages are shown in rank order, alongside their internal measurement uncertainties (^{10}Be = open circles, ^{36}Cl = filled circles). Ages which are completely enclosed by the selected component Gaussian at 2σ (including internal measurement uncertainties) are shown in red, with the remaining ages shown in grey.

Selection of the oldest component Gaussian, rather than a younger but higher probability Gaussian (e.g. 17.1 ± 1.6 ka, 18.5 ± 2.1 ka), is justified based on the relative frequency of pre- and post-depositional processes. Nuclide inheritance typically explains only a small component of geologic scatter, relative to exhumation, erosion and shielding (Zech et al., 2005; Putkonen and O'Neal, 2006; Heyman et al., 2011). Based on analysis of a large database of TCN ages from the Himalayan-Tibetan Orogen, Dortch et al. (2013) and Murari et al. (2014) estimated that the occurrence rate of inheritance was ~10%. However, while the average magnitude of inheritance was ~175% (i.e. a ~70 ka boulder on a ~40 ka moraine), the effects of inheritance were highly variable (*see* Fig. 14 in Murari et al., 2014), with some magnitudes exceeding ~300% or even ~1000% in extreme cases (i.e. a ~100 ka boulder on a ~10 ka moraine). Thus, the probability of sampling three inherited boulders on a single moraine is low (~10%^{3}= ~0.1%), while the probability of those boulders also returning exposure ages which conform to a normal distribution is also extremely low, given the varying effects of inheritance. Based on this reasoning, and for moraines deposited at or near the LGM (Dortch et al., 2013), the oldest component Gaussian that contains $\geq$ 3 ages is used to represent the age of the landform. However, this too should be regarded as a minimum age for deposition.

2 | Sensitivity analysis

Based on landform age analysis, individual boulders sampled using the Schmidt hammer were sorted into “good” and “bad” groups, which include calibrated boulder boulder ages which are within or outside the 2σ (~95%) age boundaries of the landform age respectively (*see* Fig. S3). Given the uncertainties associated with SH sampling (Aydin and Basu, 2005; Viles et al., 2011), in addition to the systematic (Jull et al., 2015; Borchers et al., 2016) and geologic uncertainties (Hallet and Putkonen, 1994) inherited from TCN dating, selection of a more precise 1σ threshold (~68%) is not justified.

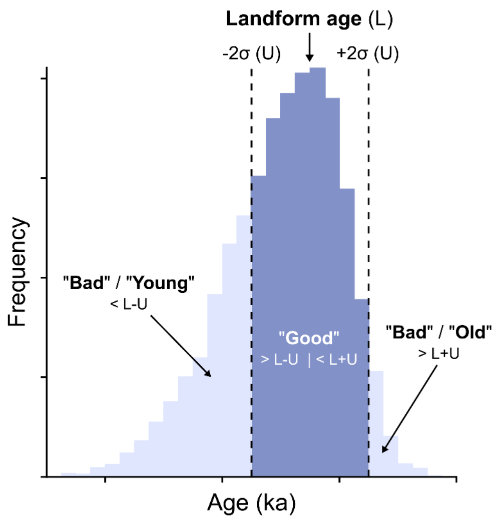

Figure S3: Schematic for boulder classification, as defined by the 2σ uncertainty bounds (U) of the landform age (L). “Good” boulders are those which fall within ± 2σ (dark purple shading), while “bad” boulders (“Young” / “Old”) are > 2σ from the landform age (light purple shading).

2.1 Methods

The logistic classification described above is ultimately dependent on the calculated landform age, which will vary depending on the choice of numeric bandwidth estimator and the size and clustering of the input dataset (Dortch et al., 2019). To evaluate the reproducibility of our results, a sensitivity analysis was undertaken as follows:

1. For each landform, random samples were drawn without replication across a range of sample sizes. The minimum sample size was set at n = 3 to reflect typical TCN sampling approaches, although collecting 5 - 6 samples is common (e.g. Pallàs et al., 2010) and larger datasets are not unheard of (Rinterknecht

et al., 2006). For each sample size, 1000 datasets were generated (e.g. $n = 3 \times 10^3$, $n = 4 \times 10^3$, ...).

2. For each dataset, we utilised an automated version of P-CAAT to calculate a simulated landform age, allowing the numeric bandwidth estimator to switch between datasets to match the size and clustering of the input data (Dortch et al., 2019). For each model run, we utilised the narrowest numeric bandwidth which P-CAAT could solve for and selected the highest probability Gaussian distribution to represent the simulated landform age.

3. For each landform and at each sample size, we recorded the number of simulated landform ages which fell within the 1σ and 2σ uncertainty bounds of the landform age calculated using the full dataset. This process was refined until 95% of simulated landform ages fell within the 1σ and 2σ thresholds.

These data provide information on the number of samples required to return the calculated landform ages within 1σ and 2σ thresholds. Simulated datasets are available on GitHub: https://github.com/matt-tomkins/moraine-crest-or-slope, while the results of this analysis are presented in Figs. S4 and S5.

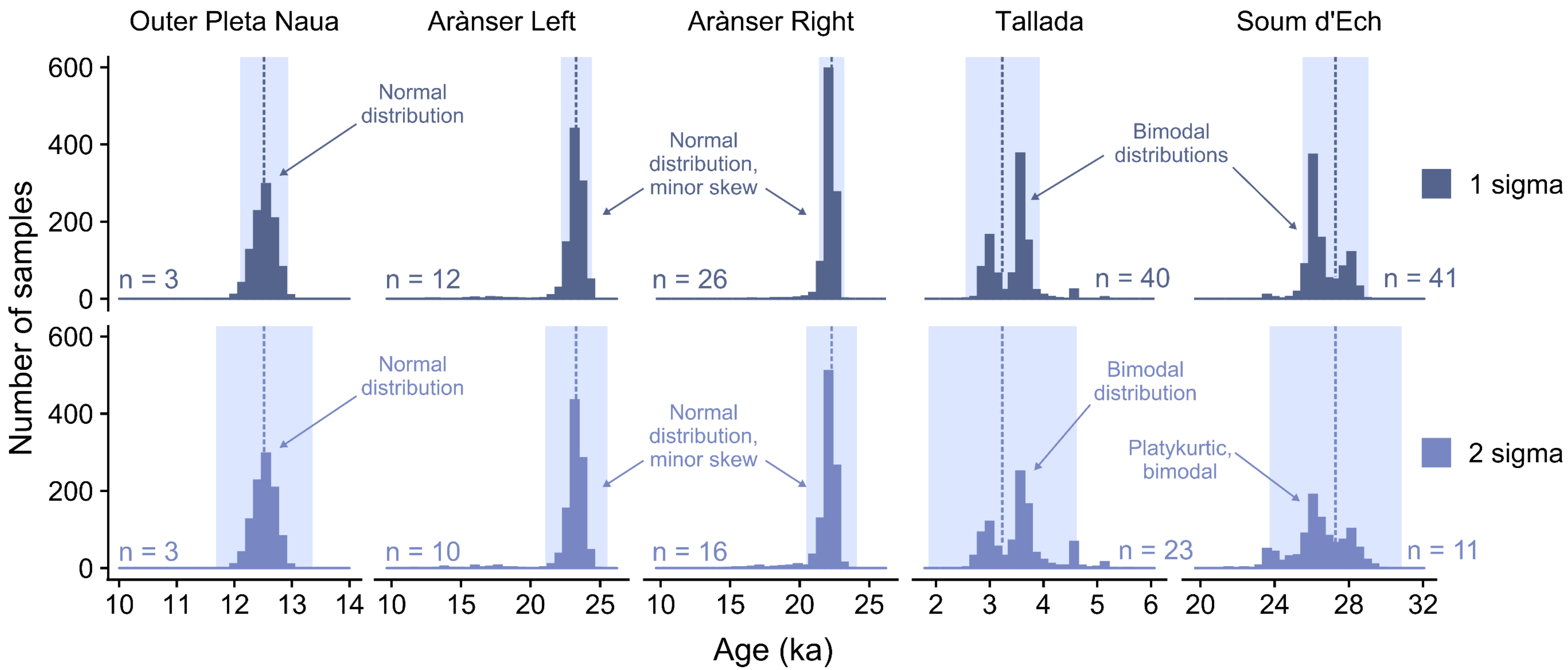

Figure S4: Histograms of simulated landform ages for the 1σ and 2σ datasets ($n = 10^3$), grouped by landform (Outer Pleta Naua, Arànser left, Arànser right, Tallada, Soum d'Ech) and by significance level (1σ, 2σ). Landform ages derived from the original dataset are denoted by vertical dashed lines, with 1σ and 2σ uncertainty bounds shown in light purple shading. The number of samples required to exceed the 1σ and 2σ thresholds is annotated.

2.2 Results

Based on the sensitivity analysis described above, there are clear differences in the number of samples required to reproduce the results obtained here (*see* Table T2). The Outer Pleta Naua landform age is the easiest to reproduce, requiring only three samples at both 1σ and 2σ. Landform ages for both the Arànser left and right moraines can be reproduced with relatively few samples at both 1σ ($n \leq 26$) and 2σ ($n \leq 16$), while both the Soum d'Ech and Tallada moraines require ≥ 40 samples to reproduce the landform age at 1σ.

Table T2: Results of sensitivity analysis

	Landform age boundary (ka)		# samples required	
Moraine	± 1σ	± 2σ	1σ	2σ
Tallada	0.68	1.36	40	23
Outer Pleta Naua	0.42	0.84	3	3
Arànser (Left)	1.12	2.24	12	10
Arànser (Right)	0.91	1.82	26	16
Soum d'Ech	1.78	3.56	41	11

These trends are largely explained by the degree of overlap between component Gaussian distributions. Both Tallada and the Soum d'Ech moraines feature lower probability component Gaussians, centred on 4.7 ± 0.9 ka and 24.4 ± 1.7 ka respectively, which exhibit considerable overlap with the highest probability component Gaussian. This trend leads to bimodal distributions of simulated landform ages (*see* Fig. S4). In contrast, there is minimal overlap between component Gaussians for the Arànser left moraine, despite the high degree of dataset skew and the large number of "bad" boulders (44%). The Arànser right moraine is intermediate in character, with clear unidirectional skew but a greater degree of overlap between the highest probability Gaussian (22.3 ± 0.9 ka) and younger lower probability component Gaussians (17.6 ± 2.9 ka; 20.9 ± 0.9 ka). This distribution explains the larger number of samples required at both 1σ and 2σ relative to the Arànser left moraine. Ultimately, as the degree of overlap between component Gaussians increases, more samples are required isolate the highest probability component Gaussian and eliminate PDE skew.

Despite this, all landform ages could be reproduced with relatively few samples at both 1σ ($n \leq 40$) and 2σ ($n \leq 26$). The number of samples required scales with the complexity of the underlying distribution, from those which are approximately normal (Outer Pleta Naua) to those which feature overlapping component Gaussian distributions (e.g. Tallada) or multi-directional skew (i.e. pre- and post-depositional skew). However, given that it is not possible to ascertain the underlying distribution a priori, a relatively large sample size is ultimately required to assess dataset skew. For most landforms, collecting a minimum of 30 samples would be a reasonable approach to estimate a depositional age within 2σ (e.g. Tomkins et al., 2018a) but more would be required to improve precision to 1σ for complex datasets or if Schmidt hammer *R*-values were being used as a basis for cosmogenic nuclide sample selection (Tylmann et al., 2018).

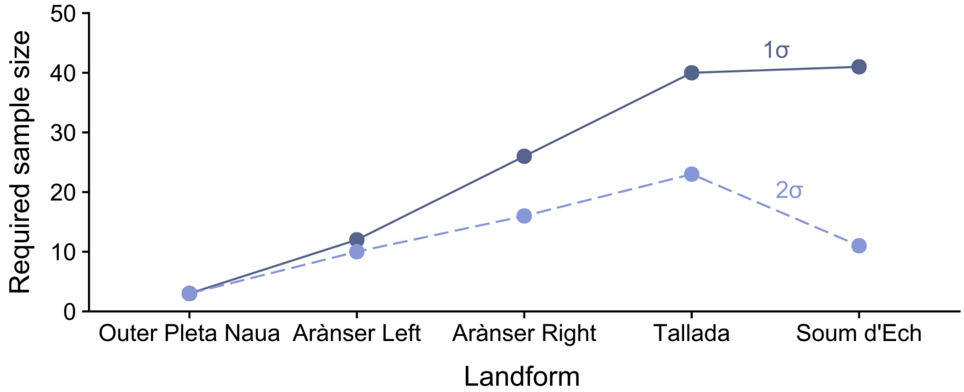

Figure S5: Minimum sample sizes based on 1σ and 2σ thresholds.

3 | Boulder characteristics

While this project was primarily focused on the spatial distribution of "good" and "bad" boulders and the relative merits of moraine crest and moraine slope sampling, a number of additional measurements were made for each sampled boulder (n = 635). These are described fully in Section 5.2 and include:

- Boulder dimensions and related metrics (*ABC* axes and ratios, ground height, surface area (m^2), volume (m^3), mass (T), sphericity and angularity).
- Surface features (presence of lichen or vegetation, degree of fracturing).
- Depositional setting (slope angle, embeddedness, underlying matrix).
- Additional spatial information (distance from the crest and base of the moraine in both absolute (m) and relative terms (%)).

Samples for cosmogenic nuclide analysis are typically selected based on the depositional context and characteristics of individual surfaces (Akçar et al., 2011; Rinterknecht et al., 2014; Palacios et al., 2019), including many of those listed above (e.g. boulder height, Heyman et al., 2016; partially embedded, Ivy-Ochs et al., 2007). While there is relatively little quantitative evidence linking these factors to poorly clustered datasets (*see* Dortch et al., 2010; Heyman et al., 2016), it is possible that these factors may modify the investigated spatial patterns.

3.1 Methods

To test this, we first utilised multivariate analysis of variance (MANOVA) for continuous predictors to assess whether there were any statistically significant differences in boulder characteristics between "good" and "bad" groups at the inter-landform scale. The underlying predictors include all those listed above, with the exception of ground height (cm) and mass (T). Ground height was a replicate of one of the *A*, *B* or *C* axis lengths, depending on the orientation of the boulder, while mass was a linear transformation of boulder volume (volume (m^3) $\times$ 2.69 g cm^3).

Next, we used logistic regression to assess the statistical significance of individual factors at both the inter-landform and intra-landform scales. For the categorical "Angularity" variable (Rounded, Sub-Rounded, Sub-Angular, Angular), we used angular boulders (A) as the reference category. This choice is appropriate because boulders entering the glacier system either subglacially or supraglacially are typically angular (i.e. sourced from rockfall or plucking), but become decreasingly angular due to glacial transport and erosion (SA $\rightarrow$ R). All other predictors were either continuous or binary. For program stability, the "Lichen" variable was removed from further analysis. Lichen presence on each boulder was recorded as either "0" (absent) or "1" (present). As lichens can colonise boulder surfaces within a few years of exposure (Putkonen and O'Neal, 2006), most sampled boulders had some degree of lichen coverage (n = 627, ~98.7%). Of those that were lichen-free (n = 8), all were classed as "Bad" (> 2σ from the landform age) and were likely recently exhumed. This distribution results in an odds ratio (OR) with 95% confidence intervals (CI) that tend towards infinity.

In addition, boulder sphericity (ψ) was removed from further logistic analysis. This was defined by Wadell (1935), and is calculated using boulder volume (V) and surface area (S) as follows:

$$\Psi = \frac{\pi^{\frac{1}{3}}(6V)^{\frac{2}{3}}}{S}$$

The distribution of boulder sphericity values is shown in Fig. S6. These data are skewed, with a median ± interquartile range of 0.77 ± 0.04. Due to the limited range of these data, with minimum and maximum values of 0.57 and 0.81 respectively, OR confidence intervals are large (95% CI = < 0.001–315,328) as they are based on values outside of the range of the data i.e. for ψ = 1, and require extrapolation based on the maximum value.

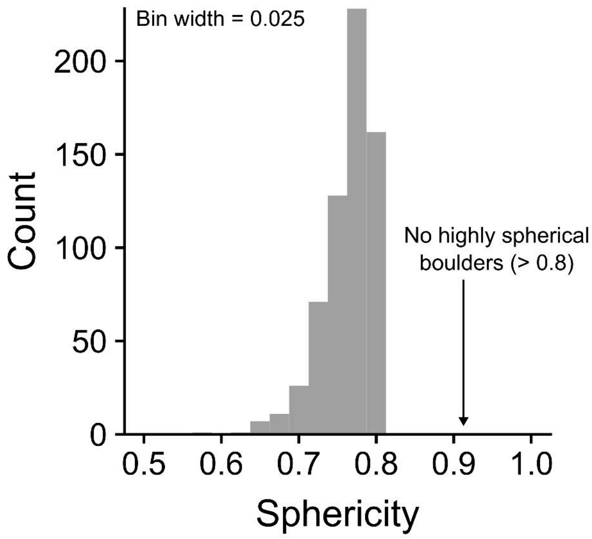

Figure S6: Histogram of boulder sphericity values (Wadell, 1935).

3.2 Results

Based on MANOVA, there is a statistically significant difference in boulder characteristics between "good" and "bad" groups at the inter-landform scale (p < 0.01).

Using logistic regression, five predictors were identified as significant (*see* Table T3). These include boulder angularity (R, SR, SA *vs*. A), the underlying slope angle (°)

and the characteristics of the moraine matrix at the sampling location (matrix support = "0" *vs.* clast support = "1"). All remaining predictors were not statistically significant ($p > 0.1$).

Table T3: Results of logistic regression of boulder characteristics ($n = 15$) at the inter-landform scale ($n = 635$), ordered by p value.

Predictor	OR (95% CI)[a]	p value
Angularity (R)	0.278 (0.143 – 0.530)	< 0.001
Angularity (SR)	0.392 (0.226 – 0.671)	0.001
Slope angle (°)	0.969 (0.943 – 0.994)	0.017
Angularity (SA)	0.584 (0.349 – 0.966)	0.038
Matrix	1.663 (0.971 – 2.882)	0.066
Height (%)	0.304 (0.050 – 1.859)	0.195
Embedded	0.528 (0.197 – 1.417)	0.204
Moss	1.725 (0.646 – 4.739)	0.282
C axis (cm)	0.992 (0.964 – 1.018)	0.539
AC ratio	2.720 (0.079 – 107.3)	0.585
B axis (cm)	0.995 (0.972 – 1.018)	0.658
Distance (%)	0.678 (0.087 – 5.371)	0.711
Surface area (m^2)	1.042 (0.717 – 1.510)	0.823
AB ratio	0.857 (0.207 – 3.672)	0.832
A axis (cm)	1.001 (0.983 – 1.020)	0.902
Fractured	0.966 (0.443 – 2.117)	0.931
Volume (m^3)	0.984 (0.652 – 1.530)	0.938

[a] Odds ratios (OR) and 95% confidence intervals (CI).

The five significant predictors were isolated and the logistic regression repeated to minimise confounding effects. The final results including odds ratios and confidence intervals are shown in Fig. S7.

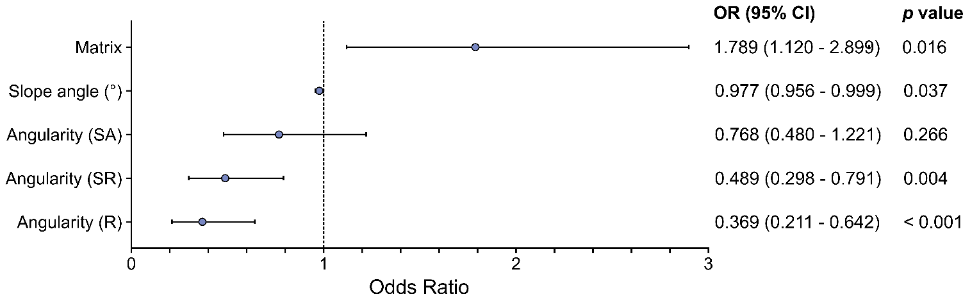

Figure S7: Significant predictors following inter-landform scale logistic regression. Forest plot of odds ratios (OR) and associated confidence intervals (95% CI). Angularity reference category = Angular (A).

The results of this analysis can be summarised as follows:

1. For every one unit change in slope angle (°), the log odds of selecting a "good" boulder *vs.* a "bad" boulder decrease by 2.3% (0.977; 95% CI: 0.956 – 0.999).

2. For every one unit change in matrix (i.e. switching from matrix to clast support; $0 \rightarrow 1$), the log odds of selecting a "good" boulder vs. a "bad" boulder increase by 78.9% (1.789; 95% CI: 1.120 – 2.899).

3. Compared to selecting an angular boulder (A), selection of a rounded (R) or sub-rounded (SR) boulder decreases the log odds of selecting a "good" boulder by 63.1% (0.369; 95% CI: 0.211 – 0.642) and 51.1% (0.489; 95% CI: 0.298 – 0.791) respectively. Selection of a sub-angular (SA) boulder has no clear effect (95% CI: 0.480 – 1.221).

These results provide some initial quantitative support for common cosmogenic nuclide sampling approaches. Based on these data, as the slope angle increases, the probability of selecting a "good" boulder decreases; a result which is consistent with a sampling focus on level areas (e.g. Ivy-Ochs and Kober, 2008) and an intuitive link between increasing slope angle and an increasing likelihood of boulder instability. In addition, selecting a clast-supported boulder *vs.* a matrix-supported boulder increases the probability of selecting a "good" boulder. This result matches evidence from the Alps for rapid stabilisation and minimal instability of clast-supported moraines (Ivy-Ochs et al., 2007).

However, the effects of boulder angularity are at odds with current approaches, which typically prioritise well-rounded boulders to minimise the likelihood of predepositional exposure (Darvill et al., 2015). In contrast, angular boulders may have originated from rockfalls, and through supraglacial transport to glacier margins or direct deposition onto moraines (Porter and Swanson, 2008), may retain a cosmogenic signal from prior exposure. This trend is not evident here, where selecting a rounded or sub-rounded boulder decreases the probability of selecting a "good" boulder compared to the reference category (A). However, this analysis is focused at the inter-landform scale and therefore does not take into account landform effects.

Of particular relevance in this case is the characteristics of the Outer Pleta Naua moraine (Pallàs et al., 2006), which appears to have stabilised rapidly after deglaciation (IQR = 0.6 ka) and consists entirely of "good" boulders (i.e. within 2σ of the landform age; n = 60). Many boulders on the Outer Pleta Naua moraine are clast-supported (~60%) while most are either angular (~60%) or sub-angular (~31%); a distribution which reflects the short transport distance from the boulder source area ($\leq$ 300 m). In turn, the characteristics of these boulders likely has a disproportionate effect on inter-landform scale analysis, and may partially explain the observed trends (e.g. angularity-matrix effects).

In turn, logistic analysis at the intra-landform scale is necessary to account for landform effects and to test whether the identified predictors (slope angle, matrix, angularity) also have explanatory power for individual landforms. However, when logistic regression was repeated for each landform, there were no statistically significant predictors for the Soum d'Ech, Tallada or Arànser right moraines (all $p > 0.05$). Analysis of the Outer Pleta Naua dataset was not possible as all boulders are classed as "good". Only the Arànser left moraine returned significant predictors ($p < 0.05$), the results of which are shown in Fig. S8. These include the extent of surface vegetation or moss (6.523; 95% CI: 1.520 – 30.35), the degree of boulder fracturing (3.507; 95% CI: 1.353 – 9.430), the underlying slope angle (0.943; 95% CI: 0.908 – 0.978) and the elevation of the boulder relative to the moraine crest (0.311; 95% CI: 0.133 – 0.703).

For the Arànser left moraine, boulders with a high degree of fracturing or surface vegetation cover were more likely to be "good". This result is consistent with sampling approaches which avoid obviously "fresh" boulders in favour of those which preserve evidence of prolonged exposure (e.g. Ivy-Ochs et al., 2007). While these predictors appear qualitatively sound, it is noteworthy that only slope angle was evident at the inter-landform scale; a result which raises uncertainty regarding their wider utility. In turn, it appears likely that landform characteristics have a greater impact on the distribution of surface exposure ages than the characteristics or depositional contexts of individual boulders. In turn, future ad hoc analyses (e.g. Dortch et al., 2010; Heyman et al., 2016) should incorporate landform characteristics as proxies for landform stability (Putkonen and O'Neal, 2006) as this may play a dominant role in determining TCN dataset skew.

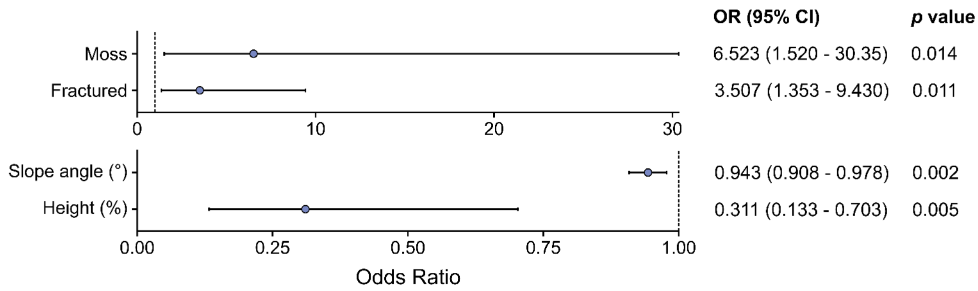

Figure S8: Significant predictors following logistic regression of the Arànser left dataset. Forest plot of odds ratios (OR) and associated confidence intervals (95% CI).

4 | Monte Carlo ODR

This section comprises a description of the Monte Carlo simulated Orthogonal Distance Regression. The full Python implementation is available on GitHub: https://github.com/matt-tomkins/moraine-crest-or-slope.

Our analytical approach is based on logarithmic orthogonal distance regression (ODR; Boggs and Rogers, 1990b), implemented in Python SciPy ("scipy.odr"; https://docs.scipy.org/doc/scipy/reference/odr.html). This approach minimises orthogonal residuals to account for the possibility of measurement uncertainties in both the independent and dependent variables. In contrast, ordinary least squares regression assumes that the independent variable is measured without error.

An unweighted approach returns prediction estimates (1σ) of ± 1.6 – 1.8 ka (calculated using the ODR covariance matrix; Boggs and Rogers, 1990a), with a distribution that corresponds to the empirical rule (~70% of calibration data within 1σ interval, ~96% within 2σ, 100% within 3σ). However, the ^{10}Be TCN ages (n = 54) and their corresponding SH *R*-values have unique measurement uncertainties which should be incorporated explicitly (TCN ± external age uncertainty; SH ± Standard Error of the Mean). This could be achieved using a weighted ODR, in which individual data points are weighted by their corresponding uncertainties. In turn, data points with high precision are weighted more heavily than those with low precision, and exert a larger influence on the final model coefficients.

However, this approach is not appropriate here because it requires unnecessary assumptions regarding weighting constants, which have a large effect on the weighting profile. For example, "scipy.odr" converts uncertainties (u) into weights as follows:

$$\frac{1}{u^2}$$

Crucially, however, weighed regression also incorporates the ratio of variabilities (λ):

$$\lambda = \frac{vX}{vY}$$

when vX is the error variance of the X data, and vY is the error variance of the Y data. In turn, using a weighted regression requires additional assumptions about the relative significance of errors. This is particularly challenging when the studied variables are measured in different units (i.e. exposure age, SH *R*-values). Finally, weighting is complicated by TCN age-uncertainty collinearity (*see* Fig. S9; as age $\nearrow$, uncertainty $\nearrow$; Ivy-Ochs et al., 2007; Dortch et al., 2019).

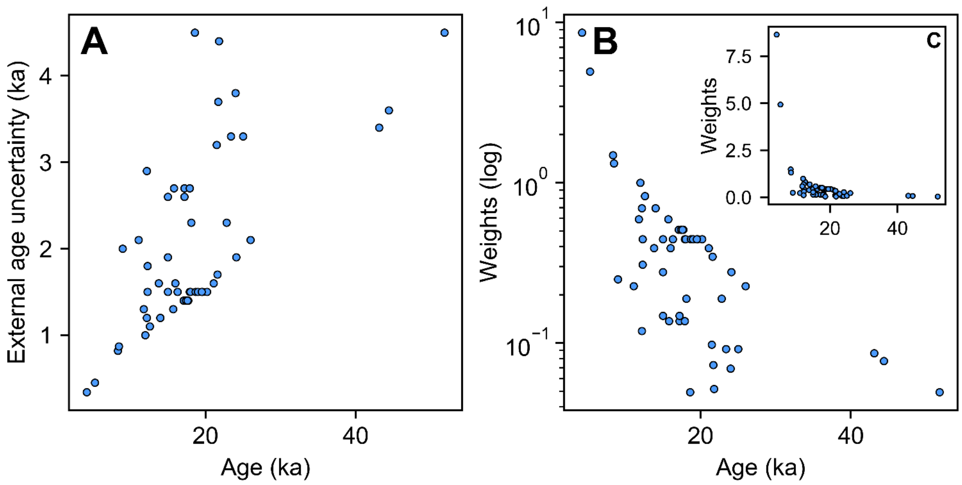

Figure S9: TCN age-uncertainty collinearity. (A) Correlation between 54 ^{10}Be TCN ages and their external uncertainties (u). Use of external uncertainties is justified here because ^{10}Be concentrations were measured at different AMS laboratories (Jull et al., 2015). Collinearity is maintained when these data are converted into weights $\left(\frac{1}{u^2}\right)$, as shown with logged (B) and unlogged axes (C).

Instead, we use a Monte Carlo style approach with 10^4 iterations to explicitly incorporate measurement uncertainties. First, random samples are drawn from a normal (Gaussian) distribution based on the input data (TCN ± external age uncertainty; SH ± Standard Error of the Mean). In turn, these data are used to construct a logarithmic ordinary least squares regression (OLS). The OLS β coefficients (slope, intercept) are used as initial parameters for the ODR model.

However, a number of input values have considerable internal measurement uncertainties ($\geq$ 10% of exposure age; *see* Fig. S10) due to the lower analytical precision of earlier Tandetron Accelerator Mass Spectrometry (Raisbeck et al., 1994). As a result, these values can vary significantly when randomised. For example, sample CAC27 can range from ~6.4 ka to ~18 ka at 2σ (12.2 ± 2.9 ka; Delmas et al., 2008; Crest et al., 2017). In turn, inclusion of these values can lead to quantitatively poor model fits. To account for this, we calculate internally studentised residuals for each OLS model and set a 2σ threshold (95%) for excluding outliers.

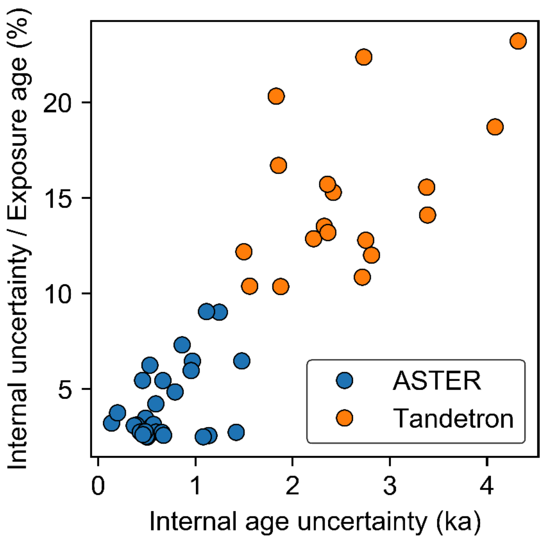

Figure S10: ^{10}Be measurement uncertainties. Internal age uncertainties plotted as a proportion of exposure age (%). ^{10}Be concentrations were measured at the Tandetron AMS facility of Gif-sur-Yvette, France (Raisbeck et al., 1994) or at the ASTER AMS facility of Aix-en-Provence, France.

For each ODR model run (n = 10^4), we record relevant model coefficients (β, covariance matrix and residuals). These values are aggregated by calculating the median; a choice which is justified based on the distribution of coefficient values (*see* Fig. S11). Slope and intercept β values and maximum model residuals conform to a normal distribution, while covariance matrix values (*see* Boggs and Rogers, 1990a) show some positive and negative skew. In turn, the median is an appropriate measure of central tendency as it is less sensitive to non-normal bias.

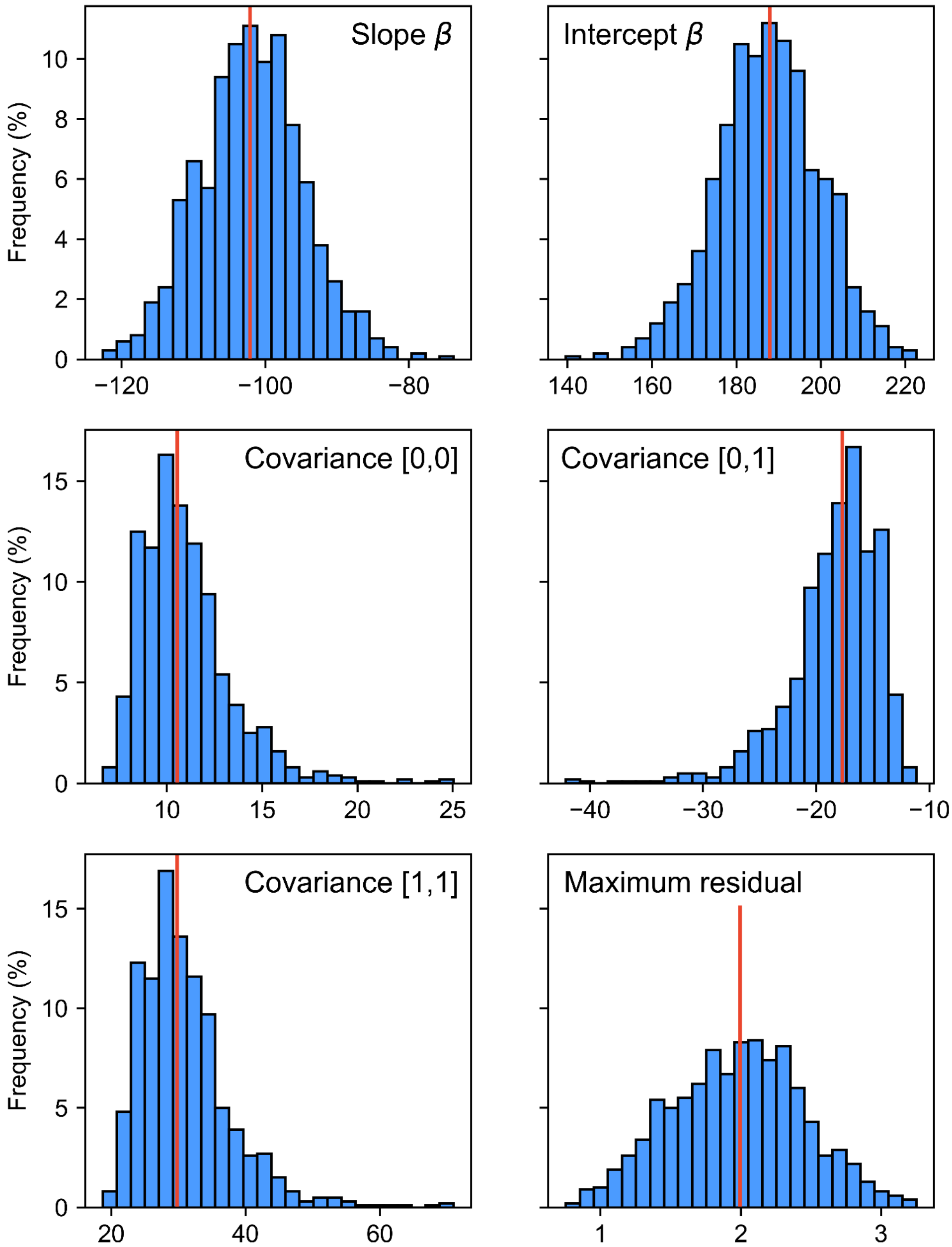

Figure S11: Simulated model coefficients ($n = 10^4$) from Orthogonal Distance Regression (β, covariance matrix, residuals)

Using these aggregated coefficients, values can be predicted as follows:

$$\beta[slope] \cdot log10(x) + \beta[intercept]$$

where x is the input value. Finally, prediction intervals can be calculated by incorporating the model derivatives, a set significance level (1σ, 2σ, 3σ) and the aggregated model coefficients (β, covariance matrix and residuals) following Boggs and Rogers (1990a).

5 | Supplementary Tables

This section provides information on the variables included in the following supplementary tables:

1. "**Supplementary_Table_1_10Be.csv**". This file includes ^{10}Be sample information used for TCN exposure age calculation. The data are listed in the format required for the CRONUS Earth Web Calculator (Version 2.0; Marrero et al. (2016), available at: http://cronus.cosmogenicnuclides.rocks/2.0/). Required variables and their descriptions are available here: http://cronus.cosmogenicnuclides.rocks/2.0/html/al-be/CRONUScalc26Al10BeTemplate.xlsx, with additional information in Section 5.1.
2. "**Supplementary_Table_2_36Cl.csv**". This file includes ^{36}Cl sample information used for TCN exposure age calculation, in the format described above. Required variables and their descriptions are available here: http://cronus.cosmogenicnuclides.rocks/2.0/html/cl/CRONUScalc36ClTemplate.xlsx, with additional information in Section 5.1.
3. "**Supplementary_Table_3_SH.csv**". This file includes sample information for all boulders sampled using the Schmidt hammer (n = 635). Variable names and calculation steps are described in Section 5.2.

5.1 Supplementary Tables 1-2

Columns [6:36](^{10}Be) and [6:84](^{36}Cl) are in the format required by the CRONUS Earth Web Calculator (Marrero et al., 2016). The remaining variables are described below:

Group

Identifier to distinguish different exposure age groups, as described below:

- "Calibration **dataset**" = The 52 ^{10}Be dated surfaces used in Tomkins et al. (2018a).
- "Calibration **outlier**" = Outliers (n = 2; *see* Fig. S12A-B), excluded by Tomkins et al. (2018a). These samples are likely compromised by prior exposure (inheritance). These include sample CAC28 from the Cometa d'Espagne cirque (Crest et al., 2017), which is proximal (~2 m) to three tightly clustered bedrock ages (c. 11 – 12 ka; mean squared weighted deviation [MSWD] = 0.094). Similarly, sample ICM04 from the Malniu catchment (Pallàs et al., 2010) is proximal (~10m) to three dated moraine boulders (c. 40 - 50 ka; MSWD = 0.945). When these

outliers are removed, both of these data sets are internally consistent (MSWD < 1).

- "Calibration **new**" = This includes two additional ^{10}Be ages from the Noguera Ribagorçana (MUL01 and MUL03; Pallàs et al., 2006) which were sampled with the Schmidt hammer during recent fieldwork (*see* Fig. S12C-D).
- "New moraine samples" = This includes all ^{10}Be and ^{36}Cl samples from the studied moraines (n = 19; Pallàs et al., 2006; Rodés, 2008; Palacios et al., 2015), of which 15 were sampled with the Schmidt hammer.

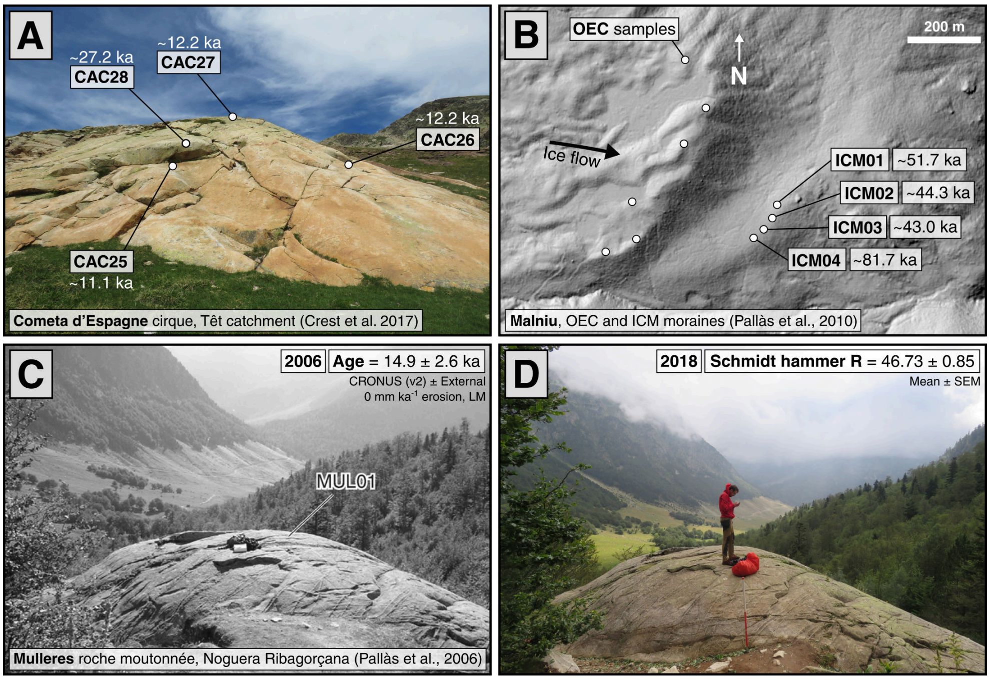

Figure S12: Outliers (A-B) and new calibration data (C-D) for the Pyrenean TCN-SH calibration curve (Tomkins et al., 2018a). (A) Outlier sample CAC28 from the Cometa d'Espagne cirque (Crest et al., 2017). (B) Outlier sample ICM04 from Malniu (Pallàs et al., 2010). (C) Sample photograph (2006) for new calibration sample MUL01 from the Noguera Ribagorçana (Pallàs et al., 2006) and its calculated surface exposure age (± external age uncertainty; CRONUS Earth Web Calculator, Marrero et al., 2016; 0 mm ka^{-1} erosion, LM scaling scheme). (D) Sample photograph for MUL01 (2018), with its corresponding mean Schmidt hammer R-value (± standard error of the mean).

Landform/Region

Name of the associated moraine, or sampling region.

Publication

Name of publication (Pallàs et al., 2006, 2010; Rodés, 2008; Delmas et al., 2008; Palacios et al., 2015; Crest et al., 2017).

Isotope

^{10}Be or ^{36}Cl.

Facility

Either Tandetron (Gif-sur-Yvette, France), ASTER (Aix-en-Provence, France) or PRIME (Purdue University, United States).

SH_Mean

Mean of 30 Schmidt hammer *R*-values. No outliers were removed following Niedzielski et al. (2009).

SH_SEM

Standard error of the mean of 30 Schmidt hammer *R*-values.

SH_Sample_Name

If this surface was resampled with the Schmidt hammer, the corresponding sample name is listed here.

CRONUS_Age [Year_Month_Day] The sample exposure age (ka), and the calculation date.

CRONUS_Internal [Year_Month_Day] The internal exposure age uncertainty (ka), and the calculation date.

CRONUS_External [Year_Month_Day] The external exposure age uncertainty (ka), and the calculation date.

5.2 Supplementary Table 3

Sample name

Unique identifier for each boulder.

Landform

Name of the associated moraine, following the prior work of Pallàs et al. (2006), Rodés (2008) and Palacios et al. (2015).

Sub-Landform

Identifier to distinguish between the outer and inner Soum d'Ech moraines.

Latitude_DD

Sample latitude in decimal degrees (°).

Longitude_DD

Sample longitude in decimal degrees (°).

Elevation_m

Sample elevation in meters above sea level (m a.s.l), as measured using a handheld GPS.

SH_Mean

Mean of 30 Schmidt hammer *R*-values. No outliers were removed following Niedzielski et al. (2009).

SH_MAD

Mean absolute deviation of 30 Schmidt hammer R-values.

SH_SEM

Standard error of the mean of 30 Schmidt hammer R-values.

TCN_Sample_Name

If this boulder has previously been dated using ^{10}Be or ^{36}Cl, the name is listed here.

Calibrated_Age_ka

Calibrated exposure age of the boulder (ka), calculated through interpolation of the TCN-SH calibration curve (*see* Fig. S13). This curve is derived from orthogonal distance regression (ODR; Boggs and Rogers, 1990b) and is based on 54 ^{10}Be dated granite and granodiorite surfaces from the Pyrenees (Pallàs et al., 2006, 2010; Delmas et al., 2008; Crest et al., 2017) and their corresponding Schmidt hammer *R*-values (Tomkins et al., 2018a). ODR allows for errors in both the independent and dependent variables. Here, we explicitly incorporate these errors (^{10}Be external age uncertainty; standard error of the mean (SEM) of the Schmidt hammer *R*-values) using a Monte Carlo style approach.

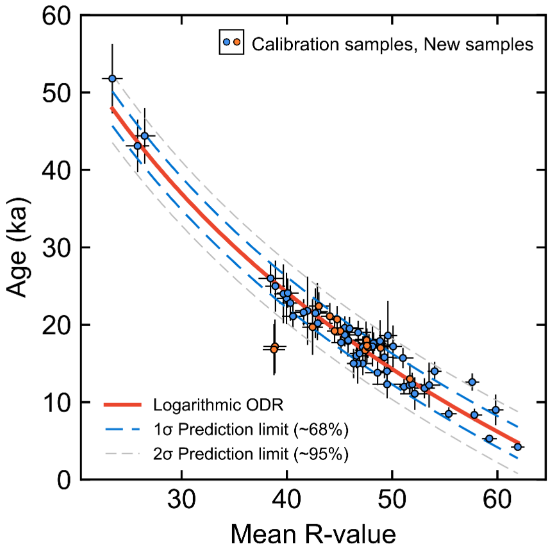

Figure S13: ODR TCN-SH calibration curve, based on 54 ^{10}Be dated granite and granodiorite surfaces from the Pyrenees (blue circles; Tomkins et al., 2018a) and calculated using Orthogonal Distance Regression (Boggs and Rogers, 1990b). New data from the studied moraines (n = 15) are shown as orange circles. Outliers (n = 2) are not shown for clarity (*see* Page 25). For all samples, vertical error bars represent the external age uncertainty, while horizontal error bars represent the standard error of the mean (SEM) of 30 Schmidt hammer *R*-values.

This approach has now been implemented on SHED-Earth (http://shed.earth), an online calculator developed to enable wider and more consistent application of our approach (Tomkins et al., 2018b).

Calibrated_Uncertainty_ka

The associated uncertainty (ka), derived from a 1σ prediction limit. This prediction limit was calculated using the ODR covariance matrix (Boggs and Rogers, 1990a).

A_axis_cm

Length of the longest boulder axis (cm).

B_axis_cm

Length of the intermediate boulder axis (cm).

C_axis_cm

Length of the shortest boulder axis (cm).

Ground_Height_cm

Maximum height of boulder above the ground (cm).

Volume_m3

Approximate volume of boulder (V, m^3), calculated as the product of the axis lengths (m) as follows:

$$V = ABC$$

Surface_area_m2

Approximate surface area of boulder (S; m^2), calculated from the axis lengths (m) as follows:

$$S = 2(AB) + 2(AC) + 2(BC)$$

Sphericity

Boulder sphericity (ψ), as defined by Wadell (1935), calculated using boulder volume (V) and surface area (S) as follows:

$$\Psi = \frac{\pi^{\frac{1}{3}}(6V)^{\frac{2}{3}}}{S}$$

Mass_Tonnes

Approximate mass of the boulder in tonnes (T), calculated using boulder volume (V) and assuming a bulk density of 2.69 g cm^3(D) as follows:

$$T = VD$$

Landform_Age_ka

Age of the landform (ka), calculated using the Probabilistic Cosmogenic Age Analysis Tool (P-CAAT Version 1.0; Dortch et al., 2019). This method utilises non-linear curve fitting and a Monte Carlo style approach to isolate component Gaussian distributions to account for positive (prior exposure) and negative skew (incomplete exposure) of age datasets. This tool is based on earlier work by Dortch et al. (2013) and Murari et al. (2014).

Landform_Uncertainty_ka

Uncertainty (ka) of the landform age. This estimate is derived from the 1σ bounds of the isolated component Gaussian distribution.

Relative_Difference_ka

Relative difference between the calibrated exposure age of the boulder and the age of the landform (ka).

Absolute_Difference_ka

Absolute difference between the calibrated exposure age of the boulder and the age of the landform (ka).

Class_95

Boulder class ("Young", "Good", "Old") as defined by the 2σ uncertainty bounds (*U*; ~95%) of the landform age (*L*, ka; *see* Fig. S3). These are distinguished as follows:

$$Young < L - U$$

$$Good \geq L - U \mid \leq L + U$$

$$Old > L + U$$

General_Class_95

Boulder class ("Good", "Bad") as defined by the 2σ uncertainty bounds (*U*; ~95%) of the landform age (*L*, ka; *see* Fig. S3). These are distinguished as follows:

$$Good \geq L - U \mid \leq L + U$$

$$Bad < L - U \mid > L + U$$

Moraine_Group

Boulder group, either moraine crest (C), the inner ice-proximal slope (IS) or the outer ice-distal slope (OS).

AB | AC_Ratio

Ratio of longest (A) to intermediate (B) or shortest axes (C).

Moss

Approximate boulder coverage by moss or surface vegetation (0%, 20%, 40%, 60%, 80%, 100%). Note, Schmidt hammer sampling was conducted in areas free of moss or surface vegetation.

Lichen

Binary category for lichen coverage (0 = Lichen absent, 1 = Lichen present). Note, Schmidt hammer sampling was conducted in lichen free areas following Matthews and Owen (2008).

Embedded

Approximate percentage of boulder embedded in ground (0%, 20%, 40%, 60%, 80%, 100%).

Angularity

Boulder morphology: Angular (A), Sub-angular (SA), Sub-rounded (SR) or Rounded (R).

Fractured

Qualitative assessment of the degree of fracturing, defined as follows:

- 0 = no fractures.
- 0.25 = minor fractures.
- 0.5 = some fractures.
- 0.75 = major fractures.
- 1 = predominantly fractured.

Note, Schmidt hammer sampling was conducted away from fractures or surface discontinuities following Williams and Robinson (1983).

Matrix

Characteristics of the underlying material, defined as follows:

- 0 = soil or sediment (i.e. matrix supported)
- 0.5 = combination of matrix and clast support e.g. sediment and boulders *or* cobbles with tightly packed sediment.
- 1 = boulders or cobbles (i.e. clast supported)

Slope_Angle_deg

Angle (°) of the underlying slope.

Distance | Height_percent

These variables provide spatially-normalised information on the relative position of each boulder. For each sampled boulder, measurement points (n = 2) were defined as the closest points along polylines digitised on (i) the moraine crest and (ii) the base of the moraine slope. In turn, distance percent (D) was calculated as follows:

$$D = \frac{C_d}{C_d + B_d}$$

where C_d is defined as the distance from the boulder to the moraine crest and B_d is defined as the distance from the boulder to the base of the moraine. Values can range from 0 for boulders located on the moraine crest to 1 for boulders on the margins of the moraine. In a similar fashion, height percent (H) was calculated as follows:

$$H = \frac{S_h - B_h}{C_h - B_h}$$

where S_h is defined as the elevation of the sampled boulder, C_h is defined as the elevation of the moraine crest and B_h is defined as the elevation of the moraine base. Values can range from 0 for boulders at the base of the moraine to 1 for boulders located on the moraine crest. It should be noted that these values are not provided for a small number of boulders on the outer ice-distal slope of the Soum d'Ech outer moraine (n = 12). This primarily reflects the subtle geomorphology of the Soum d'Ech site, where the precise boundary between the ice-distal moraine margin and the underlying non-glacial topography is not clear.

Crest | Base_distance_m

Minimum distance between the sampled boulders and polylines (.shp) digitised along the moraine crest | moraine base (m).

Crest | Base | Boulder_height_m

Elevation of the moraine crest | moraine base | sampled boulder (m a.s.l). For consistency, these measurements are derived from a ~5 m DEM from the Instituto Geográfico Nacional for the Arànser, Outer Pleta Naua and Tallada moraines. For the Soum d'Ech moraines, no data of comparable resolution are available so measurements are derived from ~30 m ASTER data (ASTER GDEM V3).

Bibliography

Akçar, N., Ivy-Ochs, S., Kubik, P. W., and Schlüchter, C. Post-depositional impacts on 'Findlinge' (erratic boulders) and their implications for surface-exposure dating. *Swiss Journal of Geosciences*, 104(3):445–453, 2011, doi:10.1007/s00015-011-0088-7.

Aydin, A. and Basu, A. The Schmidt hammer in rock material characterization. *Engineering Geology*, 81 (1):1–14, 2005, doi:10.1016/j.enggeo.2005.06.006.

Balco, G. Converting Al and Be isotope ratio measurements to nuclide concentrations in quartz. Technical report, Cosmogenic Nuclide Lab, University of Washington.

Boggs, P. T. and Rogers, J. E. The Computation and Use of the Asymptotic Covariance Matrix for Measurement Error Models. Technical Report Internal Report 89-4102, National Institute of Standards and Technology, Gaithersburg, MD, Applied and Computational Mathematics Division.

Boggs, P. T. and Rogers, J. E. Orthogonal distance regression. In *"Statistical analysis of measurement error models and applications: proceedings of the AMS-IMS-SIAM joint summer research conference held June 10-16, 1989,"*, volume 12, page 186, 1990, doi:10.6028/nist.ir.89-4197.

Borchers, B., Marrero, S., Balco, G., Caffee, M., Goehring, B., Lifton, N., Nishiizumi, K., Phillips, F., Schaefer, J., and Stone, J. Geological calibration of spallation production rates in the CRONUS-Earth project. *Quaternary Geochronology*, 31:188–198, 2016, doi:10.1016/j.quageo.2015.01.009.

Briner, J. P., Kaufman, D. S., Manley, W. F., Finkel, R. C., and Caffee, M. W. Cosmogenic exposure dating of late Pleistocene moraine stabilization in Alaska. *GSA Bulletin*, 117(7-8):1108–1120, 2005, doi:10.1130/B25649.1.

Child, D., Elliott, G., Mifsud, C., Smith, A. M., and Fink, D. Sample processing for earth science studies at ANTARES. *Nuclear Instruments and Methods in Physics Research Section B: Beam Interactions with Materials and Atoms*, 172(1):856–860, 2000, doi:10.1016/S0168-583X(00)00198-1.

Chmeleff, J., von Blanckenburg, F., Kossert, K., and Jakob, D. Determination of the 10Be half-life by multicollector ICP-MS and liquid scintillation counting. *Nuclear Instruments and Methods in Physics Research Section B: Beam Interactions with Materials and Atoms*, 268(2):192–199, 2010, doi:10.1016/j.nimb.2009.09.012.

Crest, Y., Delmas, M., Braucher, R., Gunnell, Y., and Calvet, M. Cirques have growth spurts during deglacial and interglacial periods: Evidence from ^{10}Be and ^{26}Al nuclide inventories in the central and eastern Pyrenees. *Geomorphology*, 278:60–77, 2017, doi:10.1016/j.geomorph.2016.10.035.

Darvill, C. M., Bentley, M. J., and Stokes, C. R. Geomorphology and weathering characteristics of erratic boulder trains on Tierra del Fuego, southernmost South America: Implications for dating of glacial deposits. *Geomorphology*, 228:382–397, 2015, doi:10.1016/j.geomorph.2014.09.017.

Delmas, M., Gunnell, Y., Braucher, R., Calvet, M., and Bourlès, D. Exposure age chronology of the last glaciation in the eastern Pyrenees. *Quaternary Research*, 69(2):231–241, 2008, doi:10.1016/j.yqres.2007.11.004.

Dortch, J., Saha, S., Tomkins, M. D., Murari, M. K., Schoenbohm, L. M., and Curl, D. Probability-based interpretation of terrestrial cosmogenic radionuclide ages: P-CAAT, a tool for the ages. AGU, 2019, doi:https://agu.confex.com/agu/fm19/meetingapp.cgi/Paper/502207.

Dortch, J. M., Owen, L. A., Caffee, M. W., Li, D., and Lowell, T. V. Beryllium-10 surface exposure dating of glacial successions in the Central Alaska Range. *Journal of Quaternary Science*, 25(8):1259–1269, 2010, doi:10.1002/jqs.1406.

Dortch, J. M., Owen, L. A., and Caffee, M. W. Timing and climatic drivers for glaciation across semi-arid western Himalayan–Tibetan orogen. *Quaternary Science Reviews*, 78:188–208, 2013, doi:10.1016/j.quascirev.2013.07.025.

Hallet, B. and Putkonen, J. Surface Dating of Dynamic Landforms: Young Boulders on Aging Moraines. *Science*, 265(5174):937–940, 1994, doi:10.1126/science.265.5174.937.

Heyman, J., Stroeven, A. P., Harbor, J. M., and Caffee, M. W. Too young or too old: Evaluating cosmogenic exposure dating based on an analysis of compiled boulder exposure ages. *Earth and Planetary Science Letters*, 302(1):71–80, 2011, doi:10.1016/j.epsl.2010.11.040.

Heyman, J., Applegate, P. J., Blomdin, R., Gribenski, N., Harbor, J. M., and Stroeven, A. P. Boulder height – exposure age relationships from a global glacial ^{10}Be compilation. *Quaternary Geochronology*, 34:1–11, 2016, doi:10.1016/j.quageo.2016.03.002.

Ivy-Ochs, S. and Kober, F. Surface exposure dating with cosmogenic nuclides. *E&G Quaternary Science Journal*, 57(1/2):179–209, 2008, doi:https://doi.org/10.3285/eg.57.1-2.7. Publisher: Copernicus GmbH.

Ivy-Ochs, S., Kerschner, H., and Schlüchter, C. Cosmogenic nuclides and the dating of Lateglacial and Early Holocene glacier variations: The Alpine perspective. *Quaternary International*, 164-165:53–63, 2007, doi:10.1016/j.quaint.2006.12.008.

Jull, A. J. T., Scott, E. M., and Bierman, P. The CRONUS-Earth inter-comparison for cosmogenic isotope analysis. *Quaternary Geochronology*, 26:3–10, 2015, doi:10.1016/j.quageo.2013.09.003.

Kohl, C. P. and Nishiizumi, K. Chemical isolation of quartz for measurement of *in-situ* -produced cosmogenic nuclides. *Geochimica et Cosmochimica Acta*, 56(9):3583–3587, 1992, doi:10.1016/0016-7037(92)90401-4.

Korschinek, G., Bergmaier, A., Faestermann, T., Gerstmann, U. C., Knie, K., Rugel, G., Wallner, A., Dillmann, I., Dollinger, G., von Gostomski, C. L., Kossert, K., Maiti, M., Poutivtsev, M., and Remmert, A. A new value for the half-life of 10Be by Heavy-Ion Elastic Recoil Detection and liquid scintillation counting. *Nuclear Instruments and Methods in Physics Research Section B: Beam Interactions with Materials and Atoms*, 268(2):187–191, 2010, doi:10.1016/j.nimb.2009.09.020.

Marrero, S. M., Phillips, F. M., Borchers, B., Lifton, N., Aumer, R., and Balco, G. Cosmogenic nuclide systematics and the CRONUScalc program. *Quaternary Geochronology*, 31:160–187, 2016, doi:10.1016/j.quageo.2015.09.005.

Matthews, J. A. and Owen, G. Endolithic lichens, rapid biological weathering and schmidt hammer r-values on recently exposed rock surfaces: storbreen glacier foreland, jotunheimen, norway. *Geografiska Annaler: Series A, Physical Geography*, 90(4):287–297, 2008, doi:10.1111/j.1468-0459.2008.00346.x.

Murari, M. K., Owen, L. A., Dortch, J. M., Caffee, M. W., Dietsch, C., Fuchs, M., Haneberg, W. C., Sharma, M. C., and Townsend-Small, A. Timing and climatic drivers for glaciation across monsoon-influenced regions of the Himalayan–Tibetan orogen. *Quaternary Science Reviews*, 88:159–182, 2014, doi:10.1016/j.quascirev.2014.01.013.

Niedzielski, T., Migoń, P., and Placek, A. A minimum sample size required from Schmidt hammer measurements. *Earth Surface Processes and Landforms*, 34(13):1713–1725, 2009, doi:10.1002/esp.1851.

Nishiizumi, K., Imamura, M., Caffee, M. W., Southon, J. R., Finkel, R. C., and McAninch, J. Absolute calibration of ^{10}Be AMS standards. *Nuclear Instruments and Methods in Physics Research Section B: Beam Interactions with Materials and Atoms*, 258(2):403–413, 2007, doi:10.1016/j.nimb.2007.01.297.

Palacios, D., Gómez-Ortiz, A., Andrés, N., Vázquez-Selem, L., Salvador-Franch, F., and Oliva, M. Maximum extent of Late Pleistocene glaciers and last deglaciation of La Cerdanya mountains, Southeastern Pyrenees. *Geomorphology*, 231:116–129, 2015, doi:10.1016/j.geomorph.2014.10.037.

Palacios, D., Gómez-Ortiz, A., Alcalá-Reygosa, J., Andrés, N., Oliva, M., Tanarro, L. M., Salvador-Franch, F., Schimmelpfennig, I., Fernández-Fernández, J. M., and Léanni, L. The challenging application of cosmogenic dating methods in residual glacial landforms: The case of Sierra Nevada (Spain). *Geomorphology*, 325:103–118, 2019, doi:10.1016/j.geomorph.2018.10.006.

Pallàs, R., Rodés, , Braucher, R., Carcaillet, J., Ortuño, M., Bordonau, J., Bourlès, D., Vilaplana, J. M., Masana, E., and Santanach, P. Late Pleistocene and Holocene glaciation in the Pyrenees: a critical review and new evidence from ^{10}Be exposure ages, south-central Pyrenees. *Quaternary Science Reviews*, 25(21):2937–2963, 2006, doi:10.1016/j.quascirev.2006.04.004.

Pallàs, R., Rodés, , Braucher, R., Bourlès, D., Delmas, M., Calvet, M., and Gunnell, Y. Small, isolated glacial catchments as priority targets for cosmogenic surface exposure dating of Pleistocene climate fluctuations, southeastern Pyrenees. *Geology*, 38(10):891–894, 2010, doi:10.1130/G31164.1.

Porter, S. C. and Swanson, T. W. ^{36}Cl dating of the classic Pleistocene glacial record in the northeastern Cascade Range, Washington. *American Journal of Science*, 308(2):130–166, 2008, doi:10.2475/02.2008.02. Publisher: American Journal of Science.

Putkonen, J. and O'Neal, M. Degradation of unconsolidated Quaternary landforms in the western North America. *Geomorphology*, 75(3):408–419, 2006, doi:10.1016/j.geomorph.2005.07.024.

Putkonen, J. and Swanson, T. Accuracy of cosmogenic ages for moraines. *Quaternary Research*, 59(2): 255–261, 2003, doi:10.1016/S0033-5894(03)00006-1.

Raisbeck, G. M., Yiou, F., Bourlès, D., Brown, E., Deboffle, D., Jouhanneau, P., Lestringuez, J., and Zhou, Z. Q. The AMS facility at Gif-sur-Yvette: progress, perturbations and projects. *Nuclear Instruments and Methods in Physics Research Section B: Beam Interactions with Materials and Atoms*, 92(1):43–46, 1994, doi:10.1016/0168-583X(94)95972-2.

Rinterknecht, V., Börner, A., Bourlès, D., and Braucher, R. Cosmogenic ^{10}Be dating of ice sheet marginal belts in Mecklenburg-Vorpommern, Western Pomerania (northeast Germany). *Quaternary Geochronology*, 19:42–51, 2014, doi:10.1016/j.quageo.2013.05.003.

Rinterknecht, V. R., Clark, P. U., Raisbeck, G. M., Yiou, F., Bitinas, A., Brook, E. J., Marks, L., Zelčs, V., Lunkka, J.-P., Pavlovskaya, I. E., Piotrowski, J. A., and Raukas, A. The Last Deglaciation of the Southeastern Sector of the Scandinavian Ice Sheet. *Science*, 311(5766):1449–1452, 2006, doi:10.1126/science.1120702. Publisher: American Association for the Advancement of Science Section: Report.

Rodés, *La última deglaciación en los pirineos: de superficies de exposición mediante ^{10}be, y modelado numérico de paleoglaciares*. http://purl.org/dc/dcmitype/Text, Universitat de Barcelona. Pages: 1.

Tomkins, M. D., Dortch, J. M., Hughes, P. D., Huck, J. J., Stimson, A. G., Delmas, M., Calvet, M., and Pallàs, R. Rapid age assessment of glacial landforms in the Pyrenees using Schmidt hammer exposure dating (SHED). *Quaternary Research*, 90(1):26–37, 2018, doi:10.1017/qua.2018.12.

Tomkins, M. D., Huck, J. J., Dortch, J. M., Hughes, P. D., Kirkbride, M. P., and Barr, I. D. Schmidt Hammer exposure dating (SHED): Calibration procedures, new exposure age data and an online calculator. *Quaternary Geochronology*, 44:55–62, 2018, doi:10.1016/j.quageo.2017.12.003.

Tylmann, K., Woźniak, P. P., and Rinterknecht, V. R. Erratics selection for cosmogenic nuclide exposure dating - an optimization approach. *Baltica*, 31(2):100–114, 2018, doi:10.5200/baltica.2018.31.10.

Viles, H., Goudie, A., Grab, S., and Lalley, J. The use of the Schmidt Hammer and Equotip for rock hardness assessment in geomorphology and heritage science: a comparative analysis. *Earth Surface Processes and Landforms*, 36(3):320–333, 2011, doi:10.1002/esp.2040.

Wadell, H. Volume, Shape, and Roundness of Quartz Particles. *The Journal of Geology*, 43(3):250–280, 1935, doi:10.1086/624298. Publisher: The University of Chicago Press.

Williams, R. B. G. and Robinson, D. A. The effect of surface texture on the determination of the surface hardness of rock using the schmidt hammer. *Earth Surface Processes and Landforms*, 8(3):289–292, 1983, doi:10.1002/esp.3290080311.

Zech, R., Glaser, B., Sosin, P., Kubik, P. W., and Zech, W. Evidence for long-lasting landform surface instability on hummocky moraines in the Pamir Mountains (Tajikistan) from ^{10}Be surface exposure dating. *Earth and Planetary Science Letters*, 237(3):453–461, 2005, doi:10.1016/j.epsl.2005.06.031.